Supporting Information

Solid State ESIPT Emission Switching Containing Hydroquinone and *p*-Benzoquinone Units and its Charge-Transfer Complexes

Toshitaka Tsushima,[a] Tetsu Sato,[a, b] Shun Dekura,[a, b] Takashi Takeda,[c] Ken-ichi Sakai,[d]* and Tomoyuki Akutagawa [a, b]*

[a] Graduate School of Engineering, Tohoku University, Sendai 980-8579, Japan

[b] Institute of Multidisciplinary Research for Advanced Materials (IMRAM), Tohoku University, 2-1-1 Katahira, Aoba-ku, Sendai 980-8577, Japan

[c] Faculty of Science, Shinshu University, 3-1-1 Asahi, Matsumoto 390-8621, Japan

[d] Department of Applied Chemistry and Bioscience, Chitose Institute of Science and Technology (CIST), Chitose 066-8655, Japan

Contents

23. Plot of $\ln f_p - T_p^{max\ -1}$ of **1**•TCNQ (Figure S25)

24. Imaginary part dielectric constants of **1**•TCNQ (Figure S26)

25. Temperature dependent structural changes in **1**•TCNQ (Figure S27)

Experimental section

General. Commercially available chemical reagents and solvents were used without further purification. ^{1}H (400 MHz) and ^{13}C (100 MHz) NMR spectra were recorded on a Bruker Avance III 400 NMR spectrometer. Chemical shifts (δ) are expressed in ppm relative to tetramethylsilane (^{1}H, 0.00 ppm) or residual non-deuterated solvent ($CDCl_3$; ^{13}C 39.5 ppm) as an internal standard. Elemental analyses were performed on a Microcoder JM10 at the Elementary Analysis Laboratory, Institute of Multidisciplinary Research for Advanced Materials, Tohoku University. The measurement of infrared (IR, 400-4000 cm^{-1}) spectra was carried out on KBr pellets using a Thermo Fisher Scientific Nicolet 6700 spectrophotometer with a resolution of 4 cm^{-1}. The measurement of UV-Vis spectra in DMSO and solid state were carried out in a quartz cell with an optical length of 10 mm or on KBr pellet, respectively, using Perkin Elmer Lambda 750A. The measurement of fluorescence and excitation spectra in DMSO or solid state were carried out in a quartz cell with an optical length of 10 mm or in the state of KBr pellets, respectively. Thermogravimetric analyses were performed on a Rigaku Thermoplus EVO2 instrument at a scan rate of 10 K min^{-1} under a nitrogen atmosphere.

Preparation of 2-(2,5-dihydroxyphenyl)benzothiazole (1). 15.5 g (50.0 mmol) of triphenylphosphite, 22.7 g (70.4 mmol) of tetrabutylammonium bromide (TBABr), 5.25 mL (49.1 mmol) of 2-amidobenzenethiol, and 2,5-dihydroxybenzaldehyde (6.92 g, 50.1 mmol) were weighed into a round-bottom flask (100 mL) and heated at 120°C for 1 hour. After cooling to room temperature, the mixture was extracted with ethyl acetate and water. The organic layer was separated and concentrated under reduced pressure. The obtained crude product was purified with silica gel column chromatography using a mix solvent of toluene: ethyl acetate= 95:5. The mixture was then recrystallized from toluene to afford 1.85 g (7.60 mmol, 15.2% yield) of white-colored fibrous microcrystals. Sublimation of the powdered solid yielded a yellow-colored block-shaped crystals.

^{1}H NMR (400 MHz, DMSO-d_6): δ 10.87 (s, 1H); 9.18 (s, 1H); 8.13 (d, 1H, J = 7.9 Hz); 8.04 (d, 1H, J = 7.1 Hz); 7.58 (d, 1H, J = 2.9 Hz); 7.54 (t, 1H, J = 8.0 Hz); 7.44 (t, 1H, J = 7.3 Hz); 6.92 (d, 1H, J = 8.8 Hz); 6.86 (dd, 1H, J = 8.6, 2.9 Hz); IR (KBr, cm^{-1}) 3161(br), 1603(w), 1501(s), 1457(w), 1438(m), 1315(w), 1273(m), 1239(w),1247(s), 1184(s), 1130(w), 995(m), 911(w), 845(s), 830(m), 794(m), 761(s), 742(w), 722(w), 697(w), 631(w), 525(w), 457(w), 426(w); Elemental analysis. Calc. for $C_{13}H_9NO_2S$; C: 64.18, H: 3.73, N: 5.76; Found C: 64.08, H: 3.84, N: 5.73.

Preparation of 2-(1,4-benzoquinonyl)benzothiazole (2). **1** (106.1 mg, 436 μmol) in a round-bottom flask (50 mL) was dissolved in 5 mL of ethyl acetate. Then 1 mL of an ethyl acetate solution of 2,3-dichloro-5,6-dicyano-*p*-benzoquinone (DDQ; 150.9 mg, 664.7 μmol) was added and stirred for 30 minutes. A orange powder solid (30.4 mg, 126 μmol, 28.9% yield) was obtained by vacuum filtration. Single crystals were obtained by dissolving the powder of **2** in acetone and allowing it to concentrate spontaneously, yielding red-colored block-shaped crystals.

^{1}H NMR (400 MHz, DMSO-d6): δ 8.23 (d, 1H, J = 8.8 Hz); 8.15 (d, 1H, J = 8.0 Hz); 7.64 (d, 1H, J = 2.4 Hz); 7.60 (t, 1H, J = 5.8 Hz); 7.54 (t, 1H, J = 7.7 Hz); 7.09 (d, 1H, J = 10.0 Hz); 7.03 (dd, 1H, J = 10.4, 2.4 Hz); IR (KBr, cm^{-1}) 1653(s), 1585(m), 1470(m), 1427(w), 1343(w), 1323(w), 1292(s),1249(w), 1227(w), 1165(w), 1100(m), 1069(w), 976(s), 919(m), 834(m), 784(m), 764(w), 733(w), 690(w); Elemental analysis. Calc. for $C_{13}H_7NO_2S$; C: 64.72, H: 2.92, N: 5.81; Found C: 64.43, H: 3.12, N: 5.98

Preparation of 1•BQ. *p*-BQ (107 mg, 988 micromol) was added to a solution of **1** (122 mg, 500 micromol) in ethyl acetate (4mL) in a vial (10 mL). After dissolution, 1 mL of hexane was added to precipitate a black powder. The solid was recovered by vacuum filtration and washed with hexane, yielding 120 mg (342 μmol, 68%) of black powder. Additionally, liquid-liquid diffusion using ethyl acetate as a good solvent for **1**•*p*-BQ, and hexane as a poor solvent, yielded black-colored plate-like crystals.

IR (KBr, cm^{-1}) 3228(m), 3056(w), 1641(s), 1494(s), 1436(w), 1310(w), 1273(w), 1189(m), 998(w),

877(m), 793(m), 757(w); Elemental analysis. Calc. for $C_{19}H_{13}NO_4S$; C: 64.95, H: 3.73, N: 3.99; Found C: 64.69, H: 3.94, N: 3.99.

Preparation of 1•TCNQ. TCNQ (82.5 mg, 404 μmol) and ethyl acetate (15 mL) was added to a round-bottom flask (200 mL), and the mixture was heated to 70 °C to dissolve. After addition of **1** (100.0 mg, 411 μmol), then stir vigorously with ultrasonication to precipitate a black-green colored powder. The black-green powder was filtered off using hexane under suction to afford 121.5 mg (272 μmol, 67% yield). Additionally, diffusion of **1** and TCNQ in equimolar ratio in CH_2Cl_2 yielded black plate-like crystals.

IR (KBr, cm^{-1}) 3475(m), 3057(w), 2224(s), 1583(w), 1546(s), 1484(s), 1459(s), 1433(s), 1354(w), 1337(w), 1303(m), 1275(s), 1258(s), 1221(w), 1176(s), 1125(w), 993(m), 916(m), 863(w), 849(s), 820(w), 792(s), 772(s); Elemental analysis. Calc. for $C_{25}H_{13}N_5O_2S$; C: 67.10, H: 2.93, N: 15.65; Found C: 67.37, H: 3.07, N: 15.68

Crystal structure determination. Temperature dependent crystallographic data (Table S1) were collected using a Rigaku RAPID-II diffractometer equipped with a rotating anode, fitted with a multilayer confocal optic, using Cu-Kα (λ = 1.54187 Å) radiation from a graphite monochromator. Structural refinements were carried out using the full-matrix least-squares method on F^2. Calculations were performed using Crystal Structure software packages (SHELXT and SHELXL). All parameters were refined using anisotropic temperature factors, except for those of the hydrogen atoms.

Table S1. Crystal data, data collection, and reduction parameters of **1**, **2**, and CT complexes.

Crystal	**1**	**2**	**1•BQ**	**1•TCNQ**
Chemical formula	$C_{13}H_9NO_2S$	$C_{13}H_7NO_2S$	$C_{19}H_{13}NO_4S$	$C_{25}H_{13}N_5O_2S$
Formula weight	243.28	241.26	351.36	447.46
T, K	100	293	100	100
Space group	*Pbca* (#61)	*P*-1 (#2)	*P*-1 (#2)	*P*1 (#1)
a, Å	4.6624(3)	8.4317(6)	6.7414(2)	7.0422(2)
b, Å	19.8629(9)	10.6512(7)	7.1020(3)	7.9909(2)
c, Å	23.2360(1)	11.5830(8)	17.5255(6)	8.9714(3)
α, deg	–	85.382(6)	83.108(6)	81.101(6)
β, deg	–	89.672(6)	79.950(6)	89.812(6)
γ, deg	–	89.998(6)	65.888(5)	87.172(6)
V, Å^3	2151.86(19)	1036.85(12)	753.00(6)	498.16(3)
Z	8	4	2	1
D_{calc}, g·cm^{-1}	1.502	1.545	1.550	1.491
μ, cm^{-1}	25.75	26.71	21345	17.46
Refs. meas.	4562	10927	8713	5820

Indep. refls.	1712	3703	2687	3025
Refls. Used	1712	3703	2687	3025
R_{int}	0.0983	0.1284	0.0830	0.0363
R_1 [a]	0.1621	0.1018	0.0952	0.0505
wR_2[a]	0.2233	0.2023	0.2215	0.1337
GOF	1.018	0.875	1.071	1.057
CCDC	2490538	2490539	2490541	249053

[a] $R = \Sigma||F_o| - |F_c|| / \Sigma|F_o|$ and $R_w = (\Sigma\omega(|F_o| - |F_c|)^2 / \Sigma\omega F_o^2)^{1/2}$.

Crystal	**1-TCNQ**	**1-TCNQ**
Chemical formula	$C_{25}H_{13}N_5O_2S$	$C_{25}H_{13}N_5O_2S$
Formula weight	447.46	447.46
T, K	250	350
Space group	*P*1 (#1)	*P*1 (#1)
a, Å	7.1304(10)	7.2106(8)
b, Å	8.0473(11)	8.1058(10)
c, Å	8.9775(13)	17.975(2)

α, deg	81.093(6)	81.082(6)
β, deg	89.834(6)	89.865(6)
γ, deg	87.729(6)	88.183(6)
V, Å^3	508.52(12)	1037.4(2)
Z	1	2
D_{calc}, g·cm^{-1}	1.461	1.432
μ, cm^{-1}	17.11	16.77
Refs. meas.	5769	12004
Indep. refls.	3083	6265
Refls. Used	3086	6265
R_{int}	0.0714	0.0370
R_1, [a]	0.1108	0.1641,
wR_2[a]	0.1878	0.2839
GOF	0.985	0.905
CCDC	2490540	2490988

[a] $R = \Sigma||F_o| - |F_c|| / \Sigma|F_o|$ and $R_w = (\Sigma\omega(|F_o| - |F_c|)^2 / \Sigma\omega F_o^2)^{1/2}$.

Calculations. Density functional theory (DFT) calculations for isolated molecules were performed using the Gaussian 16W software with a localized basis set for all-electron calculations. In Gaussian 16W, atomic coordinates obtained from crystal structure analysis or created using GaussView6 were used as initial structures for structural optimization, vibrational frequency calculations, and calculations of molecular orbitals and HOMO-LUMO energy levels. For absorption spectrum assignment, TD-DFT calculations were performed using the structurally optimized structures to calculate the vibrational strength and transition probability at each wavelength. Additionally, vibrational frequency analysis was performed on structures obtained from conditional structure optimization to verify the validity of the calculation results. The B3LYP/6-31G(d,p) functional/basis set was used for all calculations.

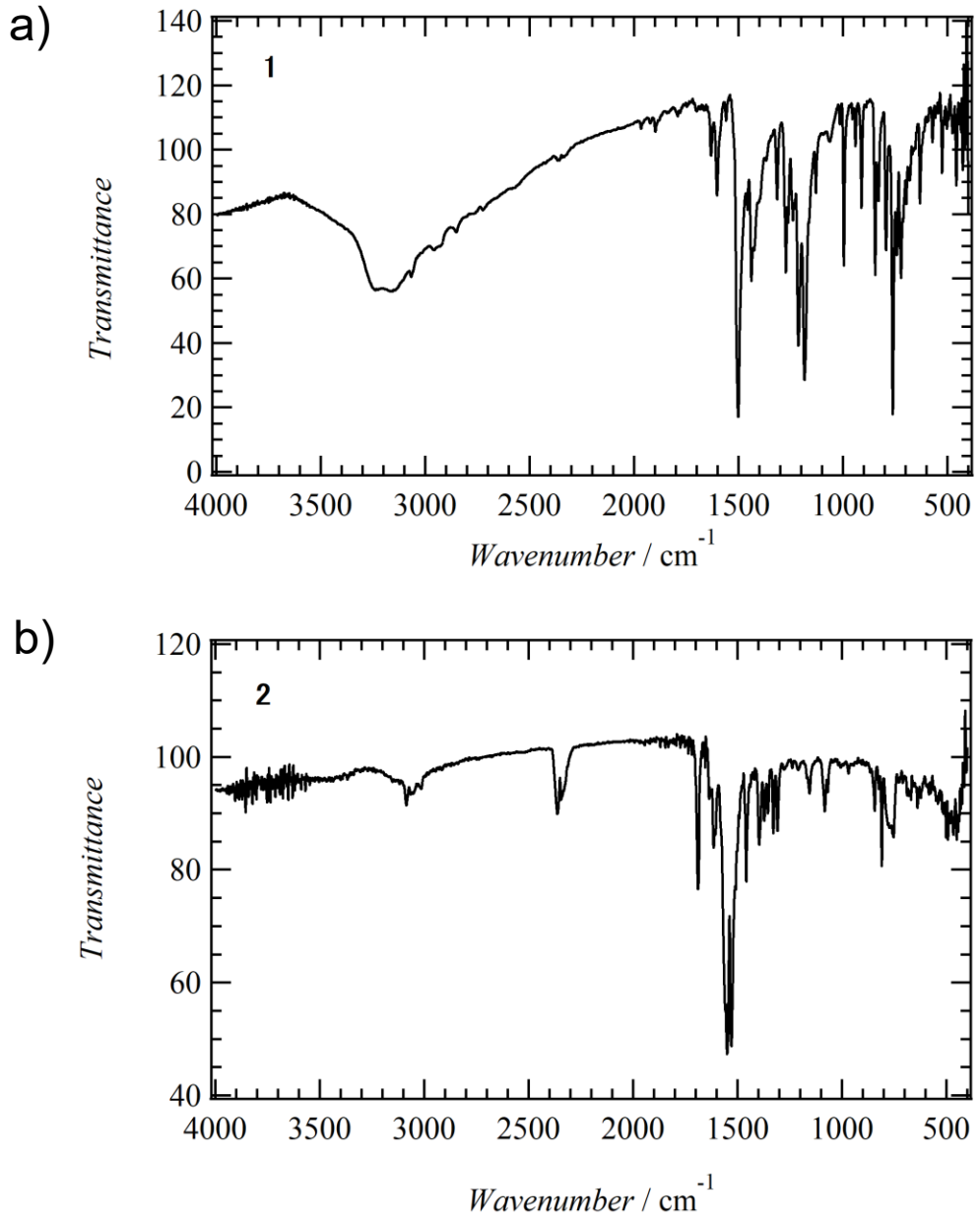

Figure S1. IR spectra of **1** and **2** using the KBr pellets.

Table S2. Optical parameter of **1** in solution.

Solvents	$\lambda_{abs,\,max,}$ nm	ε_{max}, $\times 10^4$ $M^{-1}cm^{-1}$	λ_{em}, nm	Stokes shift , cm^{-1}	λ_{ex}, nm
$CHCl_3$	365	1.33	576	10,000	380
CH_3OH	361	1.79	433	4,600	370
CH_3CN	362	1.48	410 and 586	3,200 and 10,600	370

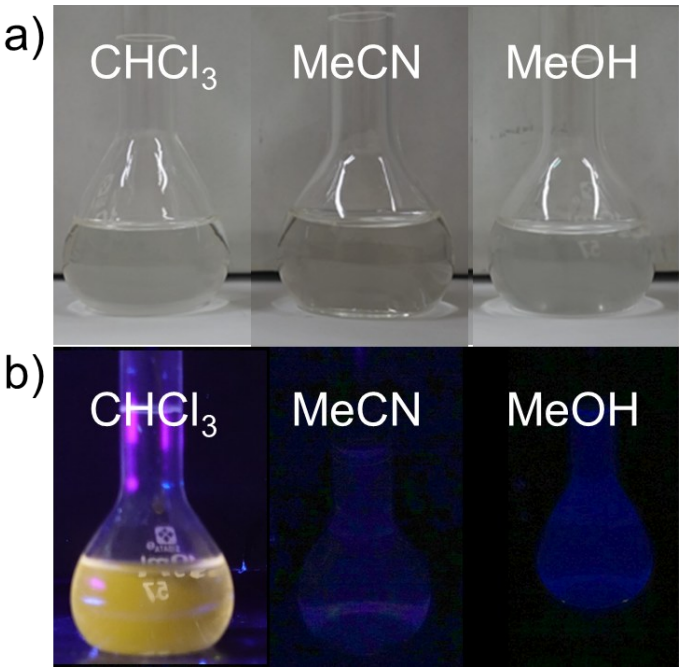

Figure S2. Photographs of solution phase **1**. a) Under sunlight and b) under the UV irradiation at wavelength of 365 nm.

Table S3. Theoretical calculations of **1** for the enol- and keto-conformations.

		1 (enol form) [a]	**1** (keto form) [a]
HOMO, eV	(eV)	−5.47	−4.91
LUMO, eV	(eV)	−1.75	−1.86
HOMO-LUMO gap, nm	(eV)	3.72	3.04
	(nm)	334	408

[a] The terms "enol" and "keto" refer to the tautomeric states of molecule **1**. Molecule **2** is the oxidized form of **1**.

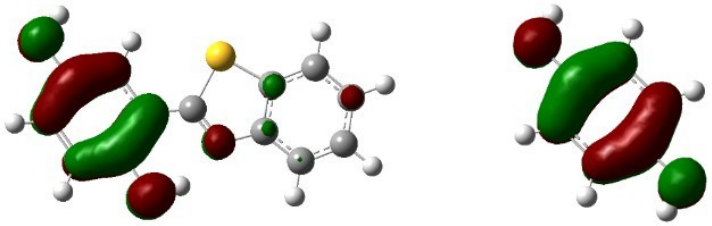

Figure S3. HOMO and energy levels of molecule **1** and H_2Q (Isovalue MO = 0.04, density = 0.0004, and laplacian = 0)

Table S4. Optical properties of **2** in solution.

Solvents	$\lambda_{abs,\ max,}$ nm	$\varepsilon_{max,}\times10^4$ $M^{-1}cm^{-1}$	λ_{em}, nm	Stokes shift, cm^{-1}	λ_{ex}, nm
$CHCl_3$	423	0.862	–	–	–
MeCN	409	0.519	–	–	–
MeOH	363	0.856	435	4,600	365

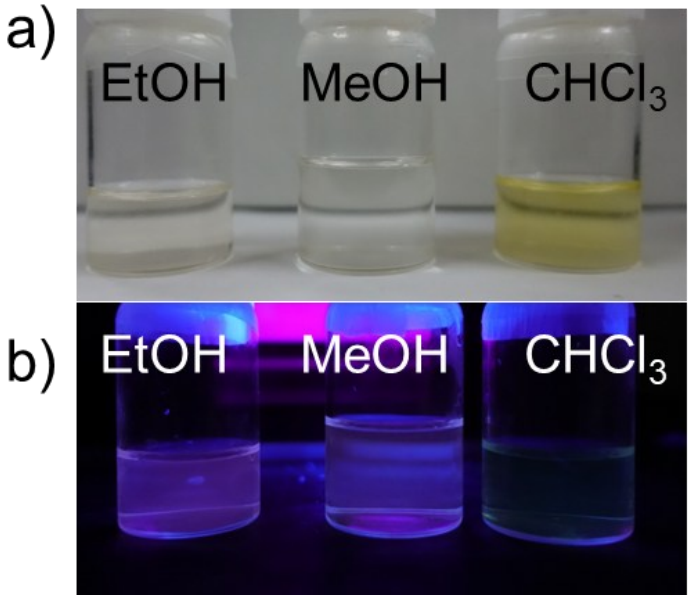

Figure S4. Photographs of solution phase **2** in C_2H_5OH, CH_3OH, and $CHCl_3$ under a) sun light and b) UV-irradiation at wavelength of 365 nm.

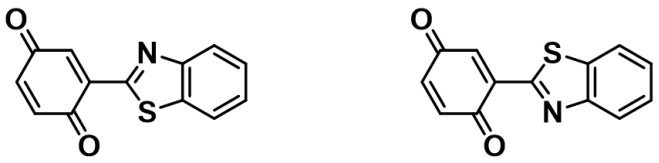

O•••S form **O•••N form**

Figure S5. Two conformations of **2** for the O•••S form and O•••N form.

Table S5. DFT calculation for O•••S form and O•••N form in molecule **2**.

	O•••S form	O•••N form
HOMO, eV	−6.49	−6.59
LUMO, eV	−3.74	−3.59
HOMO-LUMO gap, nm	2.75	3.00
	451	413

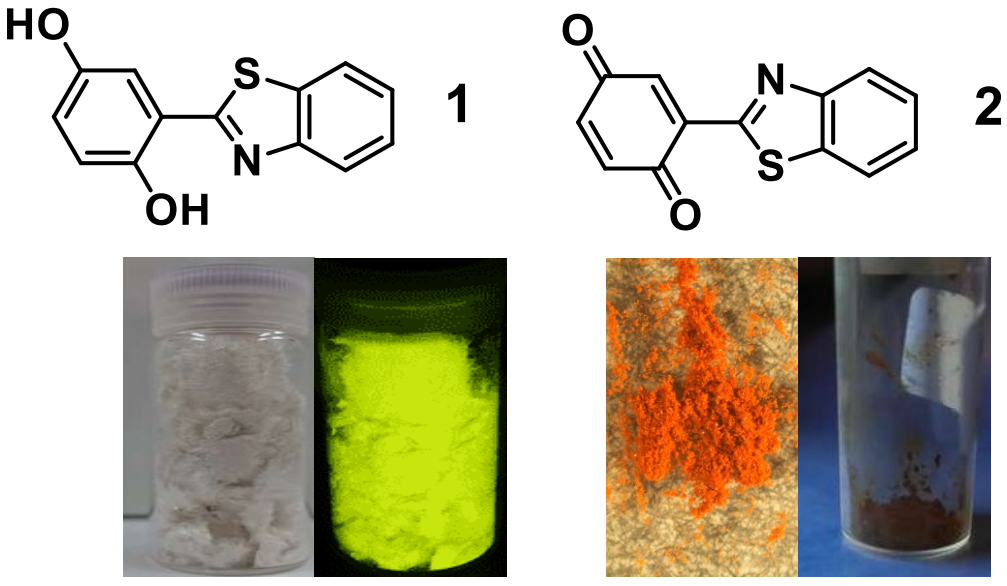

Figure S6. Solid state fluorescence of **1** and **2** under sun light and UV irradiation at wavelength of 365

nm.

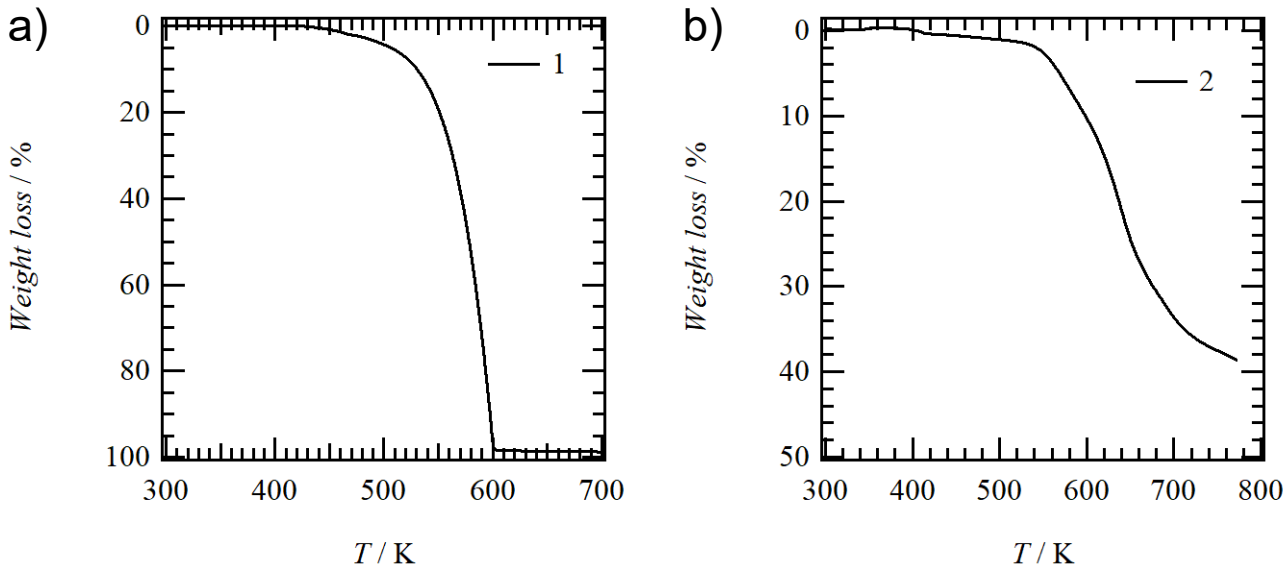

Figure S7. TG charts of **1** and **2** under the N_2 flow.

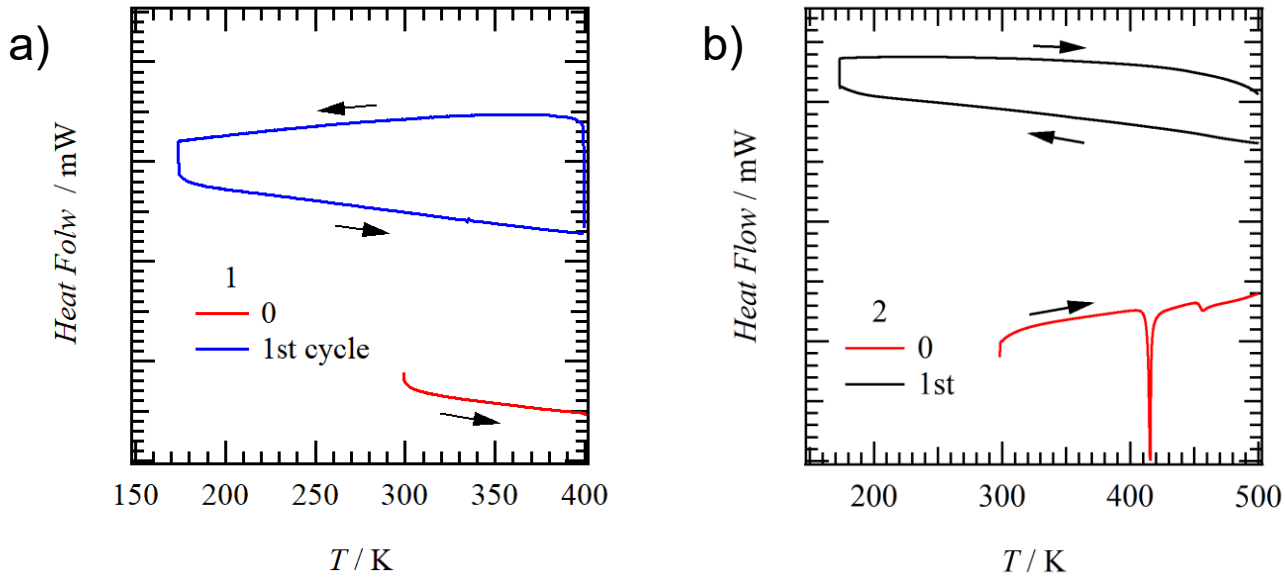

Figure S8. DSC charts of **1** and **2.**

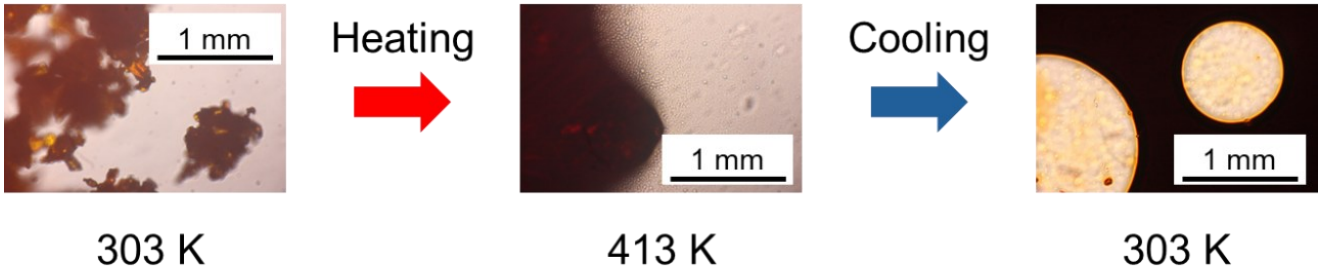

Figure S9. Photogaraps of heating and cooling process of **2.**

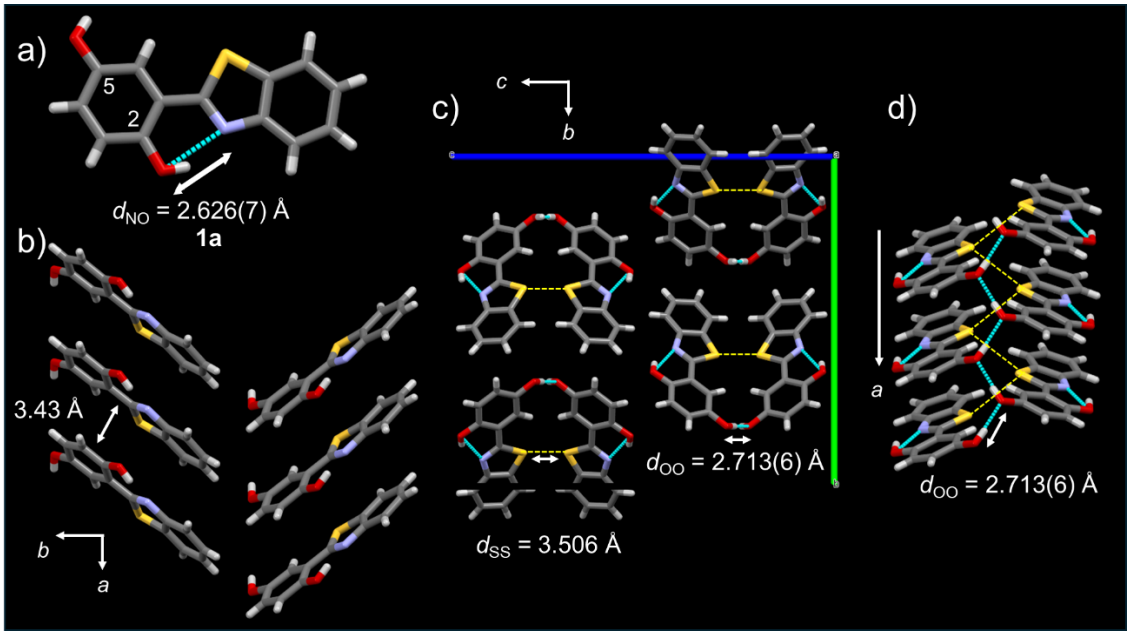

Figure S10. Crystal strucure of **1**. a) Moelcular strutcures and hydrogen-bonding dustance of **1**. b) The π-stacking and intermolecular hydrogen-bonding structure benween **1**. c) Unit cell and the interatomic distances viewed along the *a* axis. d) Average interplanat distances along the *a* axis.

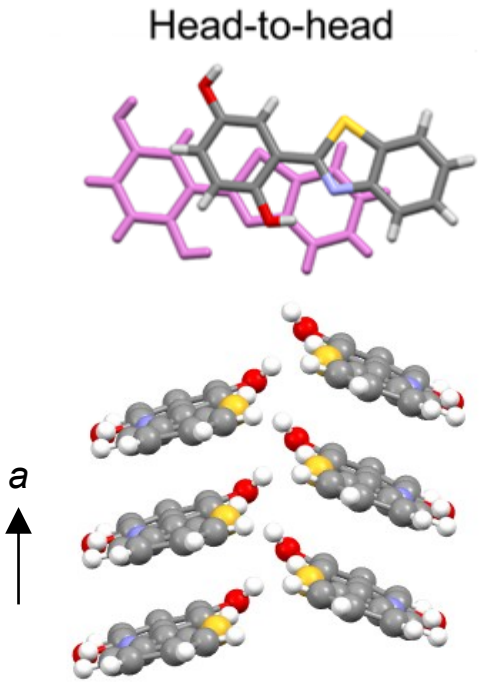

Figure S11. The head-to head π-overlappin mode and stacking manner of **1** along the *a*-axis.

Table S6. Bond lengths in **2**, H_2Q, and BQ.

	$d_{C\text{-}O}$, Å	$d_{C\text{-}C}$, Å
2	1.23(1), 1.24(1)	1.35(1), 1.38(1)
H_2Q	1.37(1)	1.38(1)
BQ	1.22(3)	1.31(1), 1.46(1)

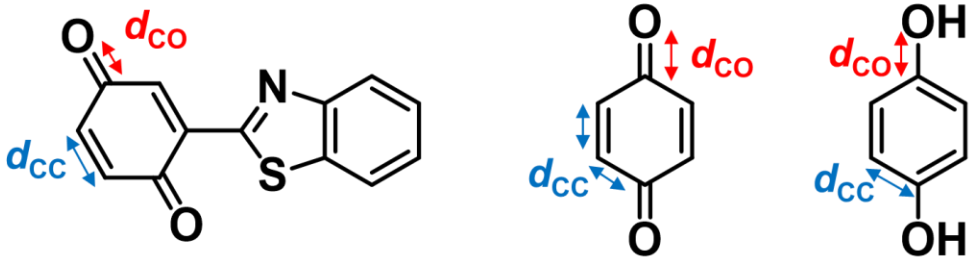

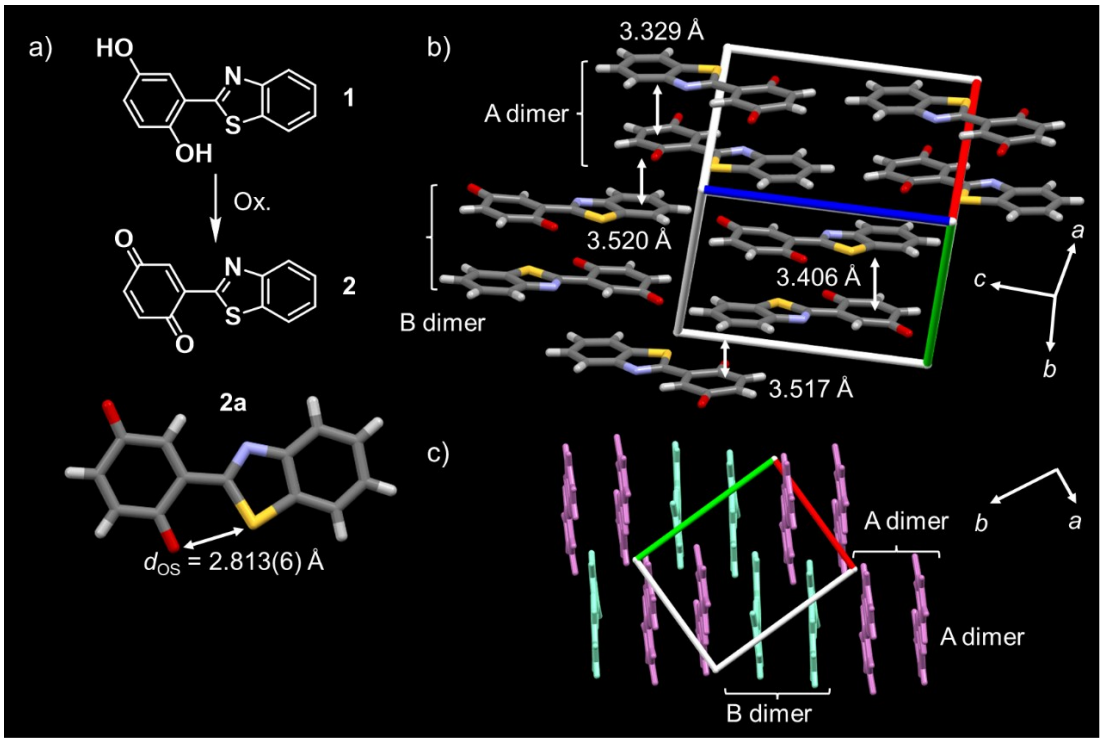

Figure S12. Crystal strucure of **2**. a) moelcular strutcures of **1** and **2**. b) Unit cell and the average interplanat distances viewed along the *a*+*b* axis. c) **A•••A** and **B•••B** dimer arrangement.

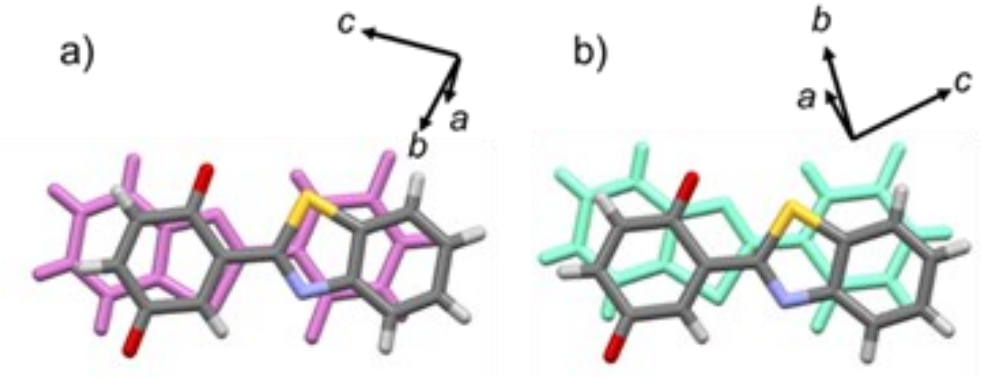

Figure S13. The head-to-tail **A**-**A** and **B**-**B** dimers in **2**.

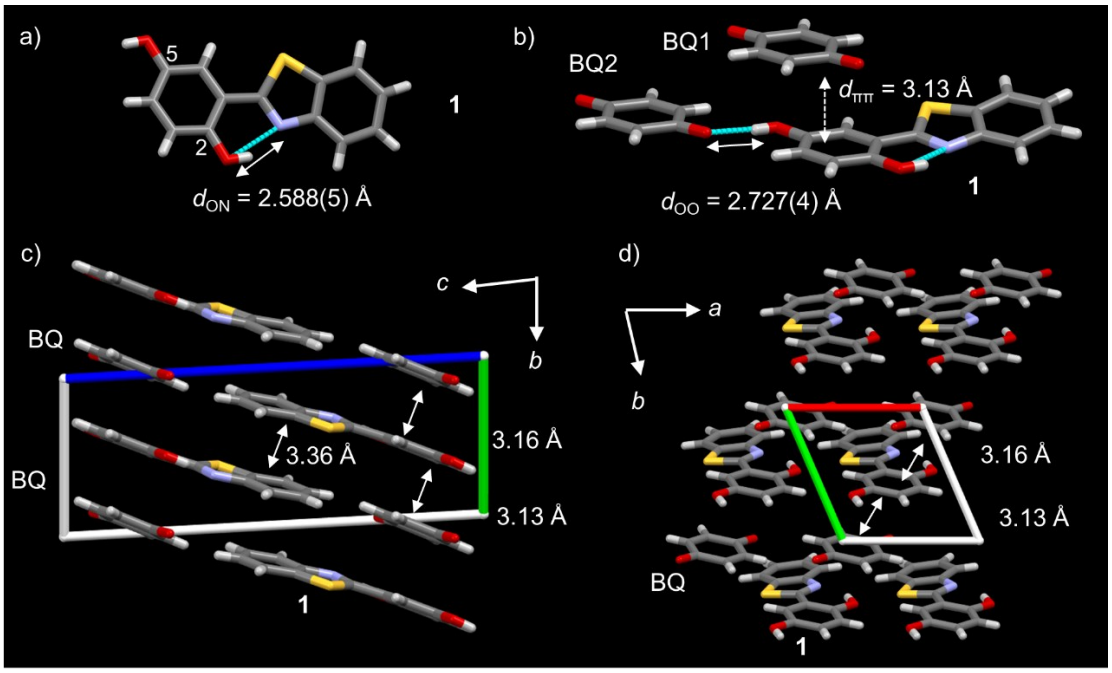

Figure S14. Crystal strucure of **1**•*p*-BQ. a) moelcular strutcures and hydrogen-bonding dustance of **1**. b) The π-stacking and intermolecular hydrogen-bonding structure benween **1** and *p*-BQ. c) Unit cell vieweda long the *a* axis. d) Unit cell vieweda long the *c* axis.

Table S7. Intermolecular hydrogen-bonding interactions ($d_{O\text{-}O}$) and average π-planar distance ($d_{\pi\text{-}\pi}$) in H_2Q•*p*-BQ and **1**•*p*-BQ crystals

	H_2Q•*p*-BQ	**1**•*p*-BQ
$d_{O\text{-}O}$, Å	2.739(6)	2.588(4)
$d_{\pi\text{-}\pi}$, Å	3.01	3.14 and 3.16

Table S8. Intramolecular bond lengths of H_2Q and *p*-BQ in the CT complexes of **1**•*p*-BQ and H_2Q•*p*-BQ.

	$d_{C\text{-}O}$, Å	$d_{C\text{-}C}$, Å
1•*p*-BQ		
1	1.36(6), 1.37(6)	1.38(5), 1.40(7)
BQ	1.22(6)	1.33(5), 1.47(5)
H_2Q•*p*-BQ		
H_2Q	1.38(1)	1.38(1)
BQ	1.23(1)	1.33(1), 1.46(2)
H_2Q [a]	1.37(1)	1.38(1)
BQ [a]	1.22(3)	1.31(1), 1.46(1)

[a] Neutral molecule.

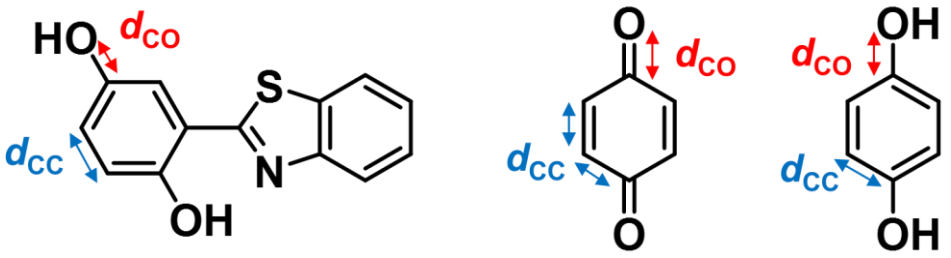

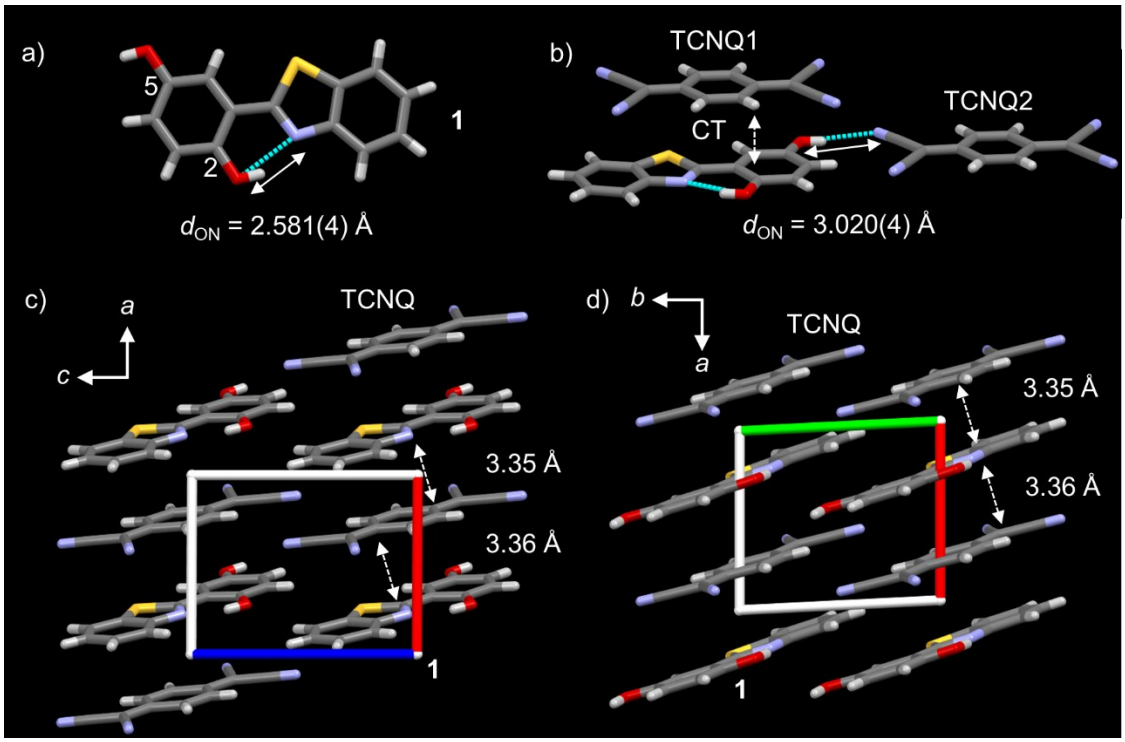

Figure S15. Crystal strucure of **1**•TCNQ. a) moelcular strutcures and hydrogen-bonding dustance of **1**. b) The π-stacking and intermolecular hydrogen-bonding structure benween **1** and TCNQ. c) Unit cell and the average interplanat distances viewed along the *b* axis. d) Unit cell and the average interplanat distances viewed along the *c* axis.

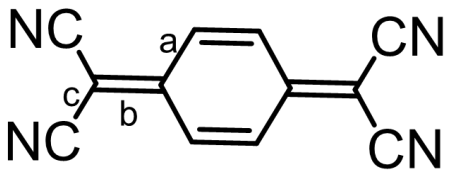

Figure S16. Bond lengths of TCNQ for the estimation of the degree of CT (δ).

$\delta = -41.67 \times [b / (a+c)] + 19.82$

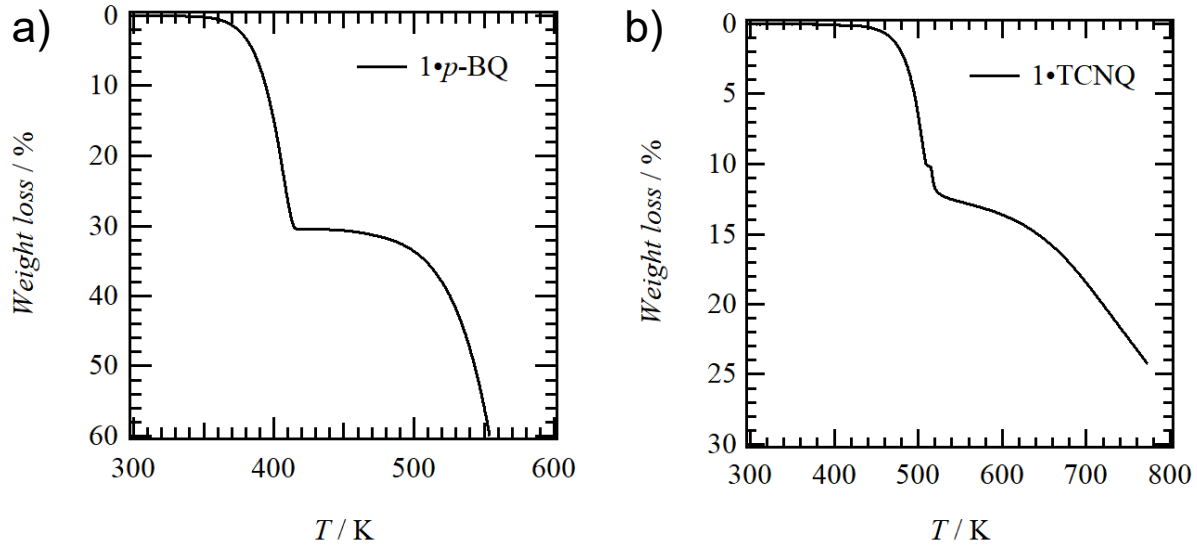

Figure S17. TG charts of **1**•*p*-BQ and **1**•TCNQ CT complexes.

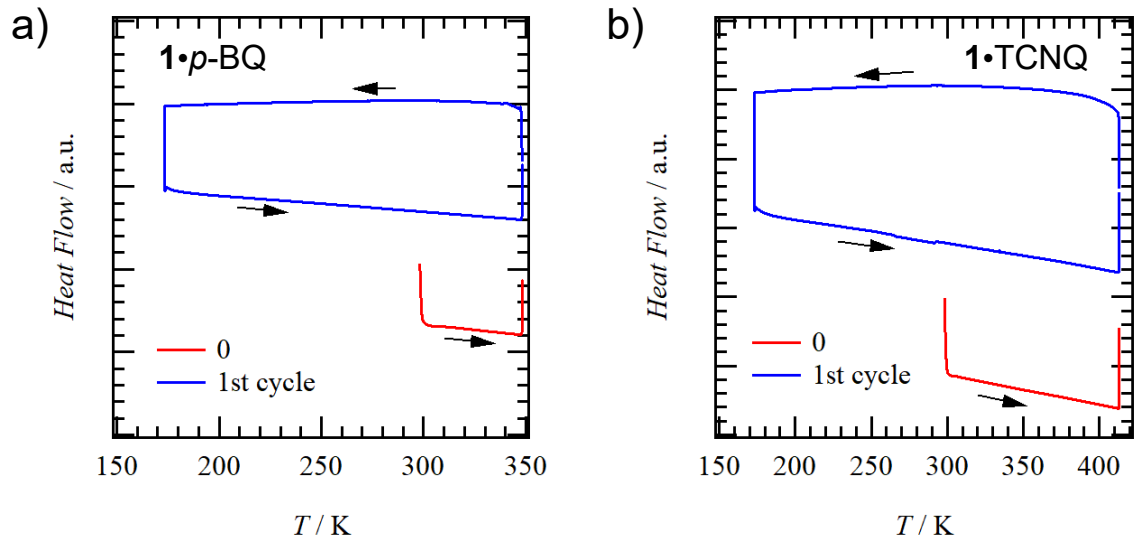

Figure S18. DSC charts of **1**•*p*-BQ and **1**•TCNQ CT complexes.

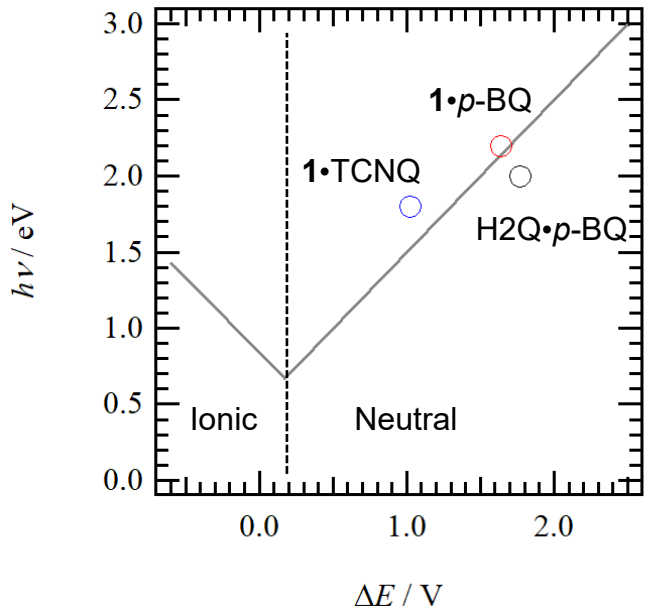

Figure S19. Plotting the CT band energy ($h\nu$) against the difference of redox potemtial (ΔE) between the oxidation potential of the donor molecule **1** and the reduction potential of the acceptor molecule on the V-shaped correlation diagram by Torrance et al (J. B. Torrance, J. E. Vazquez, J. J. Mayerle, and V. Y. Lee, *Phys. Rev. Lett*. 1980, **46**, 253-257.).

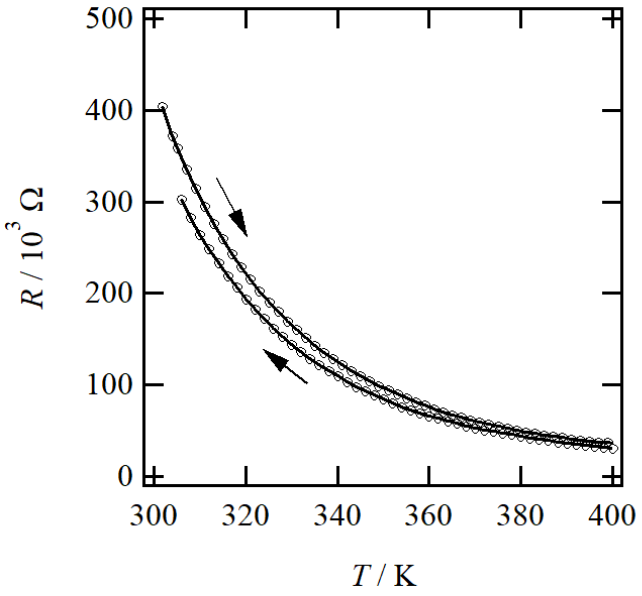

Figure S20. Temperature dependent electrical resistivity of **1**•TCNQ CT complexe using a compressed pellet.

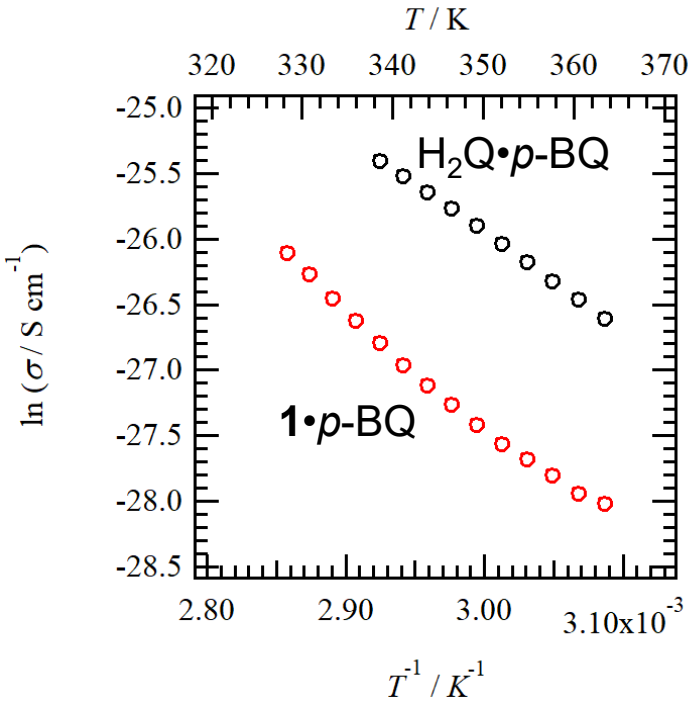

Figure S21. ln (σ / S cm^{-1}) vs T^{-1} plots of **1**•*p*-BQ and H_2Q•*p*-BQ CT complexe using a compressed pellet.

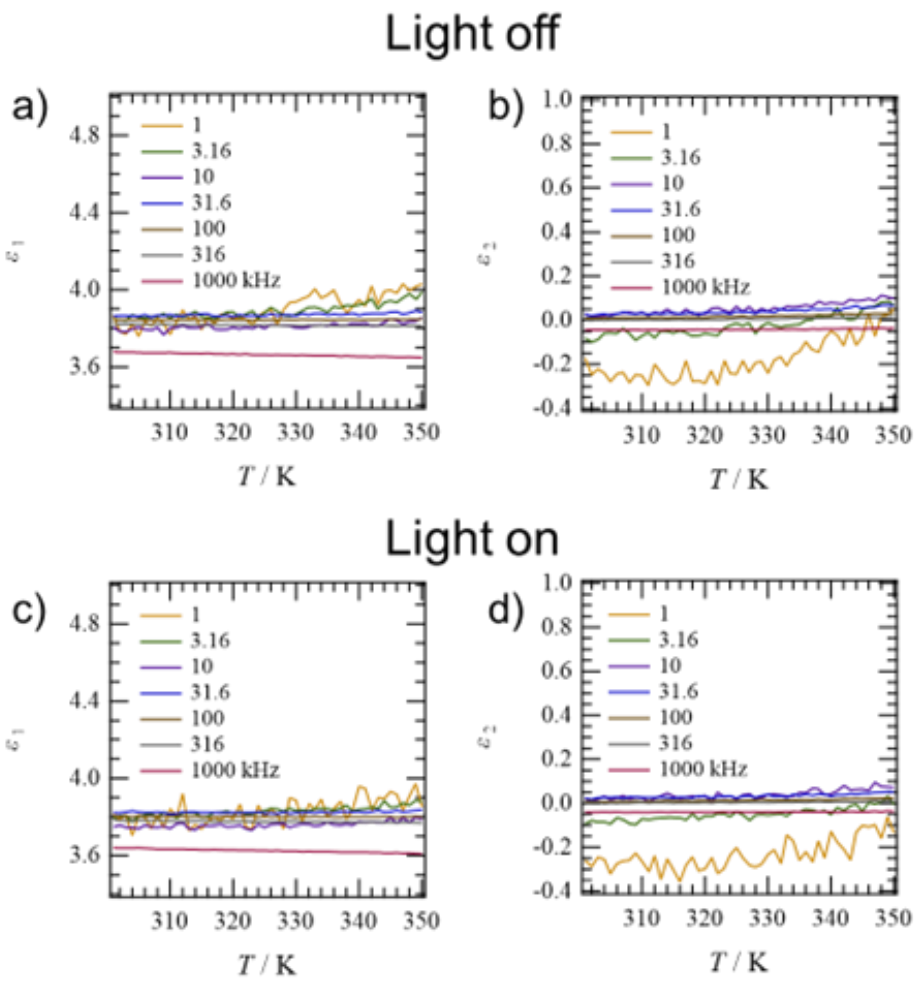

Figure S22. Real and imaginary part dielectric responses of **1**•*p*-BQ under the light a, b) OFF and c, d) ON using a compressed pellet.

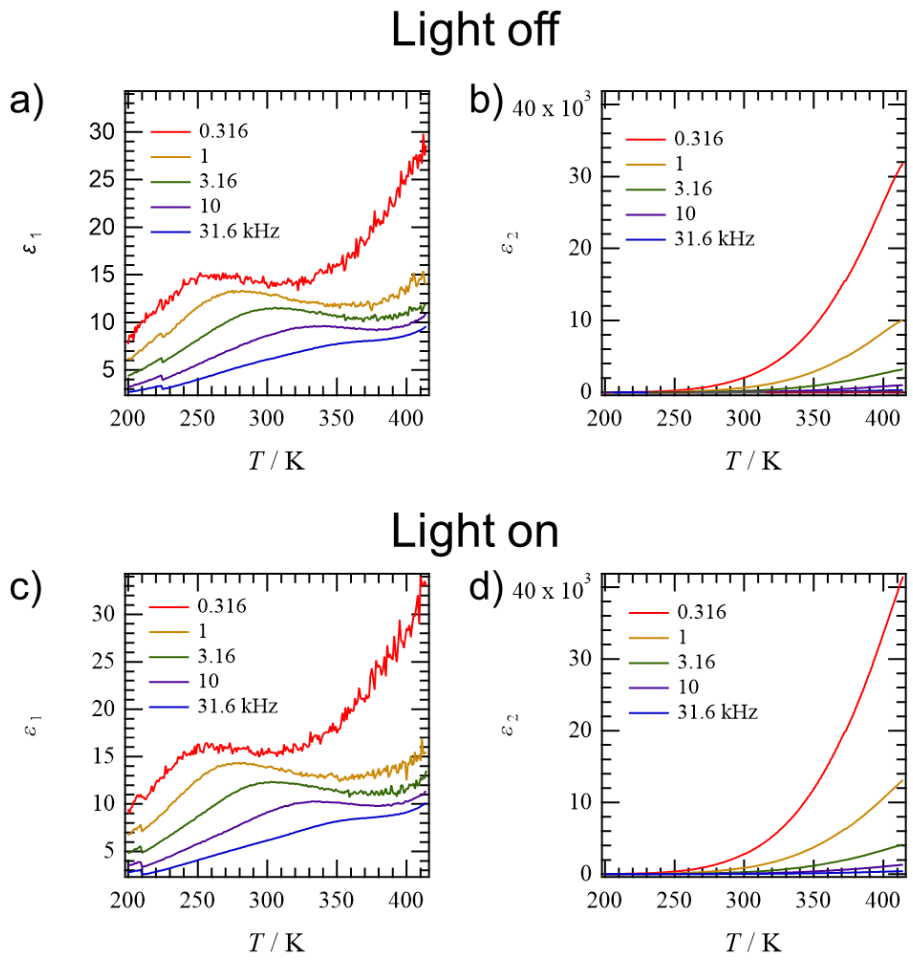

Figure S23. Real and imaginary part dielectric responses of **1**•TCNQ under the light a, b) OFF and c, d) ON using a compressed pellet.

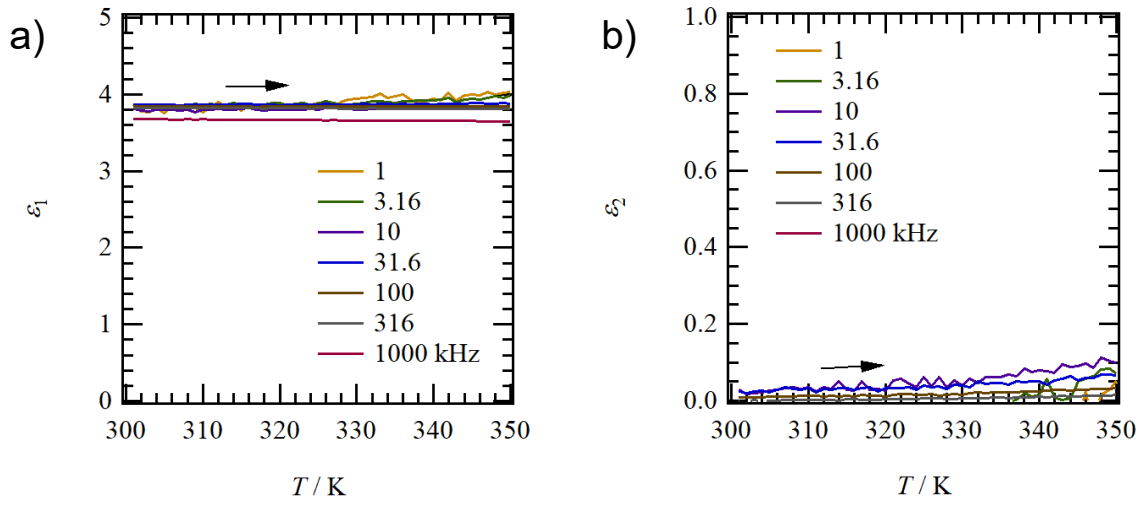

Figure S24. Temperature- and frequency-dependent a) real part and b) imaginary part dielectric constants of **1**•*p*-BQ using a compressed pellet.

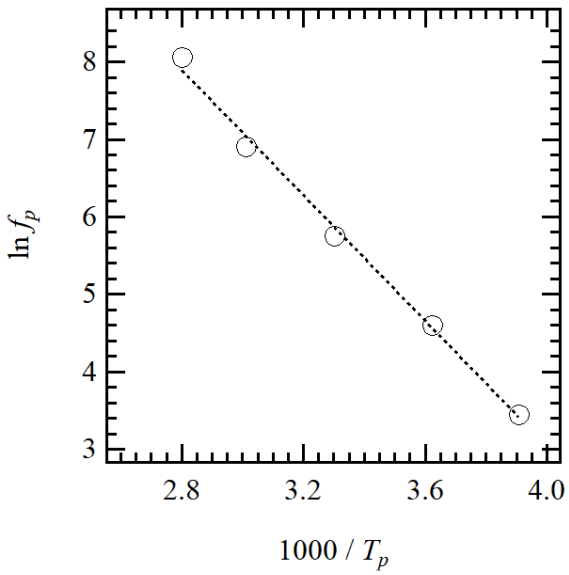

Figure S25. Plot of $\ln f_p - T_p^{max\ -1}$ of **1**•TCNQ using a compressed pellet.

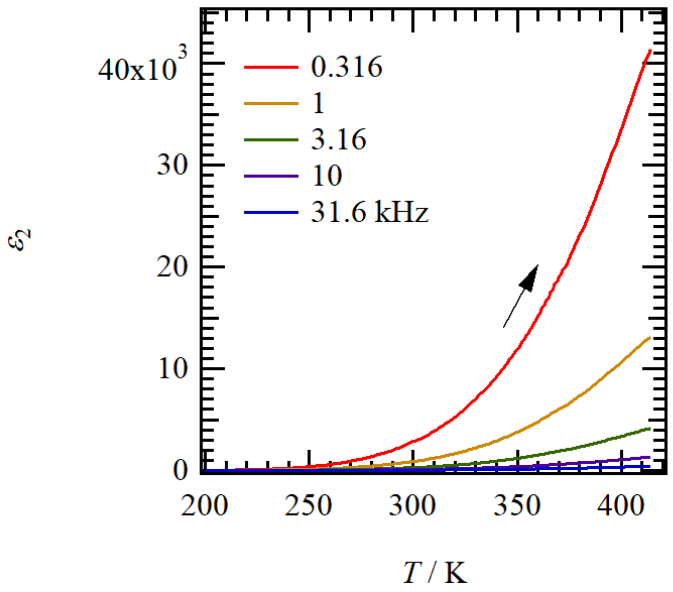

Figure S26. Temperature- and frequency-dependent imaginary part dielectric constants of **1**•TCNQ using a compressed pellet.

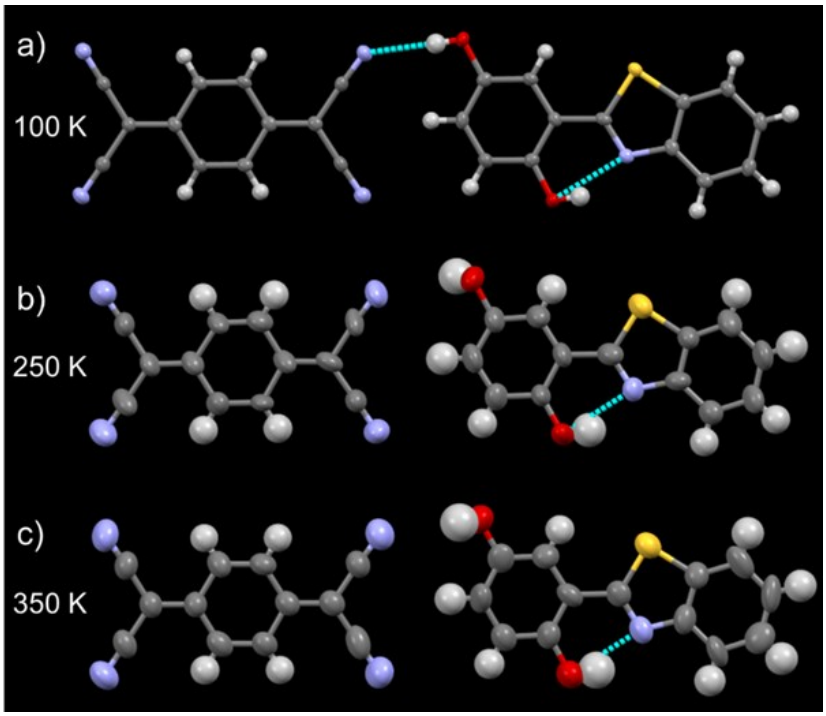

Figure S27. Temperature depndent structural changes and hydorgen-bonding properties in **1**•TCNQ.